

The Measurement of Fuel  $\rho R$  in Laser Fusion  
Targets Using Elastically Scattered Fuel Ions

S. T. Kacendar

Lab Report 132  
June 1982

The Measurement of Fuel  $\rho R$  In Laser Fusion Targets  
Using Elastically Scattered Fuel Ions

by

Steve Thomas Kacenjar

Submitted in Partial Fulfillment

of the

Requirements for the Degree  
Doctor of Philosophy

Supervised by Professor Leonard M. Goldman

Department of Mechanical and Aerospace Sciences  
College of Engineering and Applied Science

The University of Rochester  
Rochester, New York

1982

## VITAE

The author was born in Cleveland, Ohio. He graduated from Parma Senior High in 1972.

In August of 1972, he joined Case Western Reserve University for undergraduate study in the Department of Physics and completed his study with honors in May, 1976.

In July, 1976 he married and in September of that same year, joined the graduate program in the Department of Mechanical and Aerospace Sciences at the University of Rochester. In 1977, he joined the Laboratory for Laser Energetics to continue his graduate research. During his graduate years, the author has been supported by a department fellowship and a Laboratory for Laser Energetics fellowship.

He has also held a parttime faculty position at Saint John Fisher College, Department of Physics, in Rochester and held the position of teaching assistant in the Department of Mechanical and Aerospace Sciences for four semesters at the University of Rochester.

## ACKNOWLEDGEMENTS

The author is especially grateful for the guidance and valuable suggestions of his advisor, Professor Leonard M. Goldman. He has been an invaluable source of advice both during the research and writing stages of this dissertation.

The author is indebted to Dr. Stanley Skupsky for initially suggesting this research topic as well as for guidance in pursuing the theoretical issues of this research and to Dr. Alan Entenburg for his many useful discussions and support throughout this project, especially pertaining to nuclear diagnostics.

The author can not possibly acknowledge personally everyone who provided assistance during various stages of this research, but is grateful to all.

The author would like to give special thanks to Dr. Jacques Delettrez who performed and discussed many numerical simulation results of target compression; Professor Thomas Cormier, who helped in the calibration of the track detectors at the University of Rochester's Nuclear Structure Laboratory; Dr. Robert Fliecher and Dr. Brian Necholson, who initially acquainted me to the chemical processing of track detectors; George Korn, who was an invaluable help in various mechanical problems; and Beverly Hecht who spent long hours typing this dissertation.

Special thanks to my wife, Lori, for her patience and support during my graduate studies at the University of Rochester.

## ABSTRACT

The first direct measurement of the fuel  $\rho R$  in laser fusion targets has been achieved by counting the number of elastically scattered fuel ions, "knock-on particles" off 14.1 MeV DT-neutrons. Also measured for the first time was the knock-on energy spectrum which agreed well with predicted results. Both measurements required the use of thin CR-39 solid state track detectors. The presence of a proton background necessitated the development of three track criteria based on particle range and velocity to separate the knock-on deuterons and tritons from energetic protons with energies greater than 3 MeV.

Also examined here is the immediate utilization of knock-on forward-scattered deuterons to probe non-uniform fuel compressions. This requires the use of at least two track detector packages to view the target from different orientations.

A detailed discussion is also given on the future extension of the fuel  $\rho R$  measurement when target  $\rho R$  conditions exceed  $4 \text{ mg/cm}^2$ .

## TABLE OF CONTENTS

VITAE .....	ii
ACKNOWLEDGEMENTS .....	iii
ABSTRACT .....	iv
TABLE OF CONTENTS .....	v
LIST OF TABLES .....	viii
LIST OF FIGURES .....	x
I. INTRODUCTION .....	1
A. Chapter Overview .....	1
B. Fuel $\rho_R$ Determination Using Knock-On Particles .....	2
C. Alternative Methods In Measuring Fuel $\rho_R$ .....	10
1. Neutron Activation .....	11
2. Stark Broadening .....	13
3. Measurement of DT-to-DD Reaction Ratio .....	15
4. Intensity Measurement of $K\alpha$ X-Ray Lines .....	16
D. Conclusions .....	19
II. THE SIGNIFICANCE OF FUEL $\rho_R$ .....	21
A. Chapter Overview .....	21
B. Breakeven Requirements .....	22
C. Fractional Burn .....	25
D. Self-Heating .....	32
III. EXPERIMENTAL METHODOLOGY - TRACK DETECTOR ANALYSIS .....	37
A. Chapter Overview .....	37
B. Track Identification Methodology .....	38

1.	Background Sources .....	38
2.	The Spatial Coincident Criteria .....	45
C.	Track Discrimination Criteria: Experimental Verification .....	51
D.	Track Detector Calibration .....	54
1.	Section Overview .....	54
2.	The Calibration Experiment .....	56
IV.	ENERGY WINDOW DETERMINATION AND OPTIMIZATION .....	67
A.	Chapter Overview .....	67
B.	Basic Theory .....	68
C.	Energy Window Optimization - System Parameters .....	70
D.	Energy Window Optimization - Fuel Ion Ratio .....	80
V.	FUEL $\rho_R$ MEASUREMENTS - EXPERIMENTAL DATA .....	89
A.	Chapter Overview .....	89
B.	Experimental Conditions .....	90
C.	The Determination of $D^*$ Based on Experimental Data - Sample Calculations .....	93
D.	The Calculation of Fuel $\rho_R$ - Sample Calculations ....	99
E.	System Distortion in the Knock-On Spectrum .....	106
F.	Target Compression Performances .....	110
VI.	THE EXTENSION OF THE $\rho_R$ KNOCK-ON MEASUREMENT TO MODERATE $\rho_R$ CONDITIONS .....	114
A.	Chapter Overview .....	114
B.	The Examination of Two Schemes to Minimize the Effects of Uncertainty in $\sigma_{e\beta\beta}$ Due to Target Conditions ..	115

C.	Thickness Variation in Track Detectors and Its Implications on Estimating the Effective Cross Section .....	126
D.	Extension of the Ratio Method to $\rho R$ Conditions in Excess of $10 \text{ mg/cm}^2$ .....	137
VII.	THE APPROXIMATE LINE-OF-SIGHT FUEL $\rho R$ MEASUREMENT .....	141
A.	Chapter Overview .....	141
B.	Theory .....	142
C.	Applications .....	145
VIII.	SUMMARY AND CONCLUSIONS .....	152
	REFERENCES .....	157
	APPENDIX A - Solid State Track Detectors .....	160
A.	Theory .....	160
B.	Experiment Considerations .....	169
	APPENDIX B - Fractional Burn Equation .....	174
	APPENDIX C - $S/N$ Estimate Calculations .....	176
	APPENDIX D - Hydrogen Isotope Range and $D^*$ Calculations in CR-39 .....	183
	APPENDIX E - An Analysis of the Effect of multiple-Scattering of Knock-On Particles in the Tantalum Stopping Foil on the Effective Cross Section .....	193
	APPENDIX F - Derivation of the Average Neutron Path Length in a Spherical Volume of Distributed Isotropic Neutron Source .....	198
	APPENDIX G - Physics Included in Lilac .....	200



## LIST OF TABLES

Table 3.1	(n,p) Proton Background Sources.
Table 3.2	Knock-On Spectral Data.
Table 3.3	Proton Calibration Data.
Table 3.4	Etching Differences of Proton Diameters from Different CR-39 Samples.
Table 3.5	Proton - Alpha Particle Diameter Ratio from Different CR-39 Samples.
Table 5.1	Experimental Conditions and Results.
Table 5.2	Knock-On Energy Window Limits.
Table 5.3	Parameter Values and Uncertainties Used In the Calculation of Fuel $\rho R$ .
Table 6.1	Effective Cross Section Variation with Target $\rho R$ for 40 and 60 $\mu\text{m}$ thick tantalum stopping foils.
Table 6.2	Effective Cross Section Variation with Target $\rho R$ for 100 and 120 $\mu\text{m}$ thick tantalum stopping foils.
Table 7.1	Data Required for the Evaluation of Equation (6).
Table A.1	Organic SSTD Composition and Energy Thresholds.
Table C.1	Molar Chemical Composition of the Glass Tamper
Table C.2	Tamper Neutron Induced Reaction and Corresponding Cross Sections.
Table C.3	Relevant Information for the Calculation of $\eta^{eff}$ .
Table C.4	The Atomic Number Density Found in a Typical Glass Tamper.

List of Tables (continued)

Table C.5	The Calculation of $\langle M \rangle$ .
Table D.1	$dE/dx$ values for Protons in Carbon, Hydrogen, Oxygen and CR-39.
Table D.2	Range values for Protons In CR-39.

## LIST OF FIGURES

- Figure 1.1 Pictorial summary of the knock-on process.
- Figure 1.2 Knock-on energy spectrum showing the forward-scattered deuteron and triton peak.
- Figure 1.3 Knock-on diagnostic showing stopping foil, air gap, and detector arrangement.
- Figure 1.4 Pictorial summary of the radiochemistry method for measuring tamper  $\rho R$ .
- Figure 1.5 Triton beam reaction rates for various electron fuel temperatures.
- Figure 1.6  $K\alpha$  emission cross section and energy for DD-protons and DT-alpha particles as a function of the fuel seeded Z.
- Figure 2.1 Fusion reaction rate as a function of fuel ion temperature.
- Figure 2.2  $\rho R$ -fuel temperature requirements for breakeven.
- Figure 2.3 Dependence of the fractional burn as a function of temperature.
- Figure 3.1 Photograph showing intrinsic tracks associated with the initial casting of the track detector.
- Figure 3.2 Sources of laser fusion fast protons arising from various (n,p) reactions.
- Figure 3.3 Qualitative illustration of the dependence of track diameter as a function of atomic mass number.

Figures (continued)

- Figure 3.4      Qualitative illustration of spatial coincident tracks and their dependence on the atomic mass number.
- Figure 3.5      Maximum proton coincident track diameter  $D^*$ , as a function of proton range in CR-39.
- Figure 3.6      Illustration defining physical parameters associated with the initial and etched track detector.
- Figure 3.7      Experimental data showing the signature of the knock-on spectrum. The data is compared with predicted results.
- Figure 3.8      Diameter smearing of 1.5 MeV protons in CR-39.
- Figure 3.9      Hydrogen isotope track diameter as a function of  $E/A$  (experimental results).
- Figure 3.10     Alpha particle track diameter as a function of  $E/A$  (experimental results).
- Figure 4.1      Deuteron normalized differential energy distribution and its corresponding cumulative distribution.
- Figure 4.2      Triton normalized differential energy distribution and its corresponding cumulative distribution.
- Figure 4.3      Proton range in CR-39.
- Figure 4.4      Deuteron range in CR-39.
- Figure 4.5      Triton range in CR-39.

Figures (continued)

- Figure 4.6 Deuteron range in tantalum.
- Figure 4.7 Triton range in tantalum.
- Figure 4.8 Effective cross section for various tantalum thickness stopping foils as a function of CR-39 effective thickness.
- Figure 4.9 Effective cross section for various tantalum thickness stopping foils as a function of CR-39 effective thickness.
- Figure 4.10 Contour diagram of the effective cross section as a function of CR-39 and tantalum foil thickness.
- Figure 4.11 Optimization plot showing conditions to maximize the knock-on generation as a function of fuel ion ratio.
- Figure 4.12 Optimal fuel ion ratio as a function of the ratio of the effective triton-to-deuteron cross section.
- Figure 4.13 Optimal fuel ion ratio as a function of tantalum stopping foil thickness.
- Figure 5.1 Knock-on diagnostic showing retraction system.
- Figure 5.2 Photographs showing types of coincident and non-coincident tracks.
- Figure 5.3 Experimental data showing a diameter-frequency histogram of coincident and non-coincident tracks for shot number 7038.
- Figure 5.4 Histogram of non-coincident tracks from shot number 7038 to estimate  $D^*$ .

## Figures (continued)

- Figure 5.5 Maximum proton coincident track diameter as a function of the effective track detector thickness.
- Figure 5.6 Range of hydrogen isotopes in CR-39.
- Figure 5.7 Range of hydrogen isotopes in tantalum.
- Figure 5.8 Internal diameter spectrum of the knock-on triton peak using a 50  $\mu\text{m}$  tantalum foil.
- Figure 5.9 Predicted spectrum with no corrections due to diameter smearing and energy straggling compared with the measured experimental spectrum.
- Figure 5.10 Predicted spectrum with corrections due to diameter smearing and energy straggling compared with the measured experimental spectrum.
- Figure 5.11 Simulation result showing temporal variation in the neutron production rate and the fuel  $\rho\text{R}$ .
- Figure 6.1 The effective cross section as a function of tamper  $\rho\text{R}$  for various stopping foil thicknesses.
- Figure 6.2 Energy acceptance window variation as the tamper  $\rho\text{R}$  is increased.
- Figure 6.3 Correlation of the effective cross section with the DD-proton energy loss.
- Figure 6.4 Illustration showing the ratio method for correcting for  $\rho\text{R}$  distortions in the knock-on spectrum.

### Figures (continued)

- Figure 6.5 Correlation of the  $S(120)/S(100)$  ratio to the effective cross section for the 120  $\mu\text{m}$  stopping foil system.
- Figure 6.6 Correlation of the  $S(40)/S(60)$  ratio to the effective cross section for both the 40 and 60  $\mu\text{m}$  stopping foil systems.
- Figure 6.7 Illustration defining parameters related to thickness variations across the track detector.
- Figure 6.8 The effective cross section as a function of CR-39 thickness for the 40 and 60  $\mu\text{m}$  stopping foil systems.
- Figure 6.9 The effective cross section as a function of CR-39 thickness for the 100 and 120  $\mu\text{m}$  stopping foil systems.
- Figure 6.10 Calculated effective cross section variation due to detector thickness uncertainty using ratio method.
- Figure 6.11 Calculated effective cross section variation due to detector thickness uncertainty using ratio method.
- Figure 6.12 Calculated effective cross section variation as a function of DD-proton energy loss with spread resulting from detector thickness uncertainty.
- Figure 6.13 Systematic uncertainty effect on the effective cross section.
- Figure 6.14 Correlation of the  $S(40)/S(60)$  ratio to the effective cross section for the 40  $\mu\text{m}$  stopping foil system.
- Figure 6.15  $\rho R \cdot Y_n$  threshold values as a function of target  $\rho R$ .

## Figures (continued)

- Figure 7.1 Knock-on collection geometry.
- Figure 7.2  $\phi$  integration cases in the evaluation of  $dn/d\theta$ .
- Figure 7.3  $dn/d\theta$  distribution as a function of  $\theta$  when collecting with a 50  $\mu\text{m}$  thick tantalum stopping foil. Both deuterons and tritons produce coincident tracks.
- Figure 7.4  $dn/d\theta$  distribution as a function of  $\theta$  when collecting with a 120  $\mu\text{m}$  and 140  $\mu\text{m}$  thick tantalum stopping foil. Only forward-scattered deuterons produce coincident tracks.
- Figure A.1 Latent track formation in track detectors. The breaking of hydrocarbon chains by a charged particle.
- Figure A.2 Threshold damage conditions showing typical bragg curves for different ions in solid state track detectors.
- Figure A.3 Track formation as a function of time. The importance of the track and bulk etch rates on track formation is illustrated.
- Figure A.4 Illustration of track parameters required to derive equation A.5.
- Figure A.5 Track formation of an obliquely incident-charged particle.
- Figure A.6 Dependence of track diameter as a function of temperature in CR-39.
- Figure A.7 Experimental chemical etching set-up.



Figures (continued)

- Figure A.8      Electrochemical etching set-up.
- Figure A.9      Tree discharge phenomena in electrochemically-etched track detectors.
- Figure E.1      Multiple-scattering angle vs. fraction of range traversed by protons, deuterons and alpha particles.
- Figure E.2       $\langle \theta^2 \rangle$  vs. deuteron energy for a 50 and 120  $\mu\text{m}$  thick tantalum stopping foil.
- Figure E.3      Illustration defining  $\ell$  and  $T$  used in the derivation of equation E.8.

## INTRODUCTION

### A. Chapter Overview

During future laser fusion studies, such aspects as self-heating of the fuel by DT alpha particles and fuel ion depletion by thermonuclear burn will become of increasing importance. These aspects depend strongly upon the fuel  $\rho R$  (Rho-R), a parameter which is the product of the fuel density and its confinement radius. This product is also a critical parameter for determining the proximity to thermonuclear ignition. A discussion on the significance of fuel  $\rho R$  will be explored in greater detail in Chapter 2. In this chapter the author will discuss a diagnostic which has been developed and implemented to measure this parameter. The measurement relies on counting the number of elastically scattered deuterons and tritons, "knock-on particles," off the by 14.1 MeV DT neutrons. These knock-on particles are recorded on solid state track detectors.<sup>1</sup>

Much of the data analysis relies on a basic understanding of how solid state track detectors record charged and neutral particles. Therefore, in Appendix A a brief discussion on how track detectors work is given for those readers not familiar with this type detector.

In Chapter 3, the basic issue of how this measurement is performed is addressed. Here a discussion of various backgrounds and how they are discriminated from knock-on particles is presented.

Chapter 4 will examine more carefully the details on how the knock-on energy window is determined. Also in this chapter a discussion on optimal fuel ion concentration will be presented.

This is followed by Chapter 5 with experimental data where the method is applied and fuel  $\rho R$  determined. Included here is a discussion of various measurement uncertainties entering into the estimate of  $\rho R$ .

Next in Chapter 6 a discussion is given on the usefulness of this method for target  $\rho R$  conditions where significant distortion in the knock-on spectrum can occur. It will be shown that the target  $\rho R$  cannot exceed about  $.1 \text{ g/cm}^2$  (approximately ignition conditions) in order for the knock-on particles to have sufficient energy to escape the target.

This is followed by Chapter 8, which explores a possible application of this diagnostic to measure fuel compression nonuniformities during the time of neutron production.

The dissertation concludes with Chapter 9, which summarizes the important aspects presented in the work.

#### B. Fuel $\rho R$ Determination Using Knock-On Particles

This section will serve to orient the reader to the underlying physics describing how knock-on particles give information of the fuel  $\rho R$ . It will then examine the experimental method developed to record and count the knock-on particles. Also a qualitative discussion will be given on the problems raised by this methodology. Lastly, this section will examine the limitations of the measurement due to particle slowdown under high target  $\rho R$  conditions. No attempt is made in this section to examine quantitatively the many technical

issues associated with this method or its accompanying limitations. This discussion is reserved to later chapters in this dissertation.

Qualitatively, this method relies on the fact that the fuel  $\rho R$  is directly proportional to the number of knock-ons produced. This is illustrated in Figure 1.1. In particular, the total number of knock-ons  $Q$ , is given by

$$Q = (\sigma_d n_d R + \sigma_t n_t R) Y_n \quad (\text{I-1})$$

where  $\sigma_d$  and  $\sigma_t$  are the  $(n, d)$  and  $(n, t)$  elastic cross sections,  $Y_n$  is the neutron yield and, the  $n_d$  and  $n_t$  are the deuterium and tritium ion densities. In this equation it is assumed that the neutron mean free path  $(n\sigma)^{-1}$  is much larger than the fuel dimensions  $R$ . If :  $n_d = n_t = n_o$  and  $M_p$  is the mass of a proton, then the ion density can be related to the fuel density by

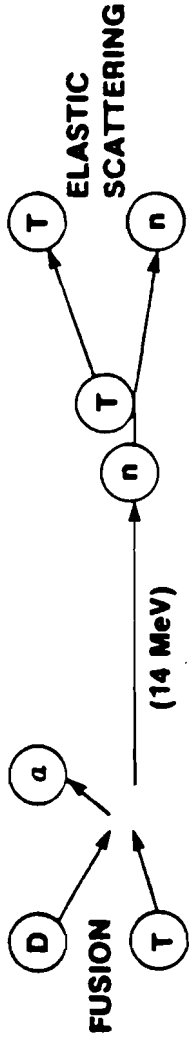
$$n_o = \frac{\rho}{5M_p} \quad (\text{I-2})$$

Thus, the fuel  $\rho R$  can be expressed as

$$\rho R = \frac{5M_p}{\sigma_D + \sigma_T} \frac{Q}{Y_n} \quad (\text{I-3})$$

$$= 5.422 \frac{Q}{Y_n} \quad (\text{I-4})$$

**MEASURING FUEL  $\rho_R$  WITH KNOCK-ONS (example)**



- The Number of Elastic Collisions by  $n$  on  $T$   
 $= \sigma n_T \langle R \rangle \approx .1 \rho \langle R \rangle$

- Total Number of Knock-On Tritons Detected

$$Q = \sigma n_T \langle R \rangle \cdot Y \cdot F$$

Where

$Y$  = Neutron Yield

$F$  = Fraction of Knock-Ons in the Energy Window of The Track Detector

$$\rho \langle R \rangle \approx \frac{10Q}{Y \cdot F} \text{ g/cm}^2$$

- Determining  $F$  Is The Major Theoretical Uncertainty.  
 $F$  Is Sensitive to The Temperature and  $\rho_R$  of The Target.

TC727

Figure 1.1

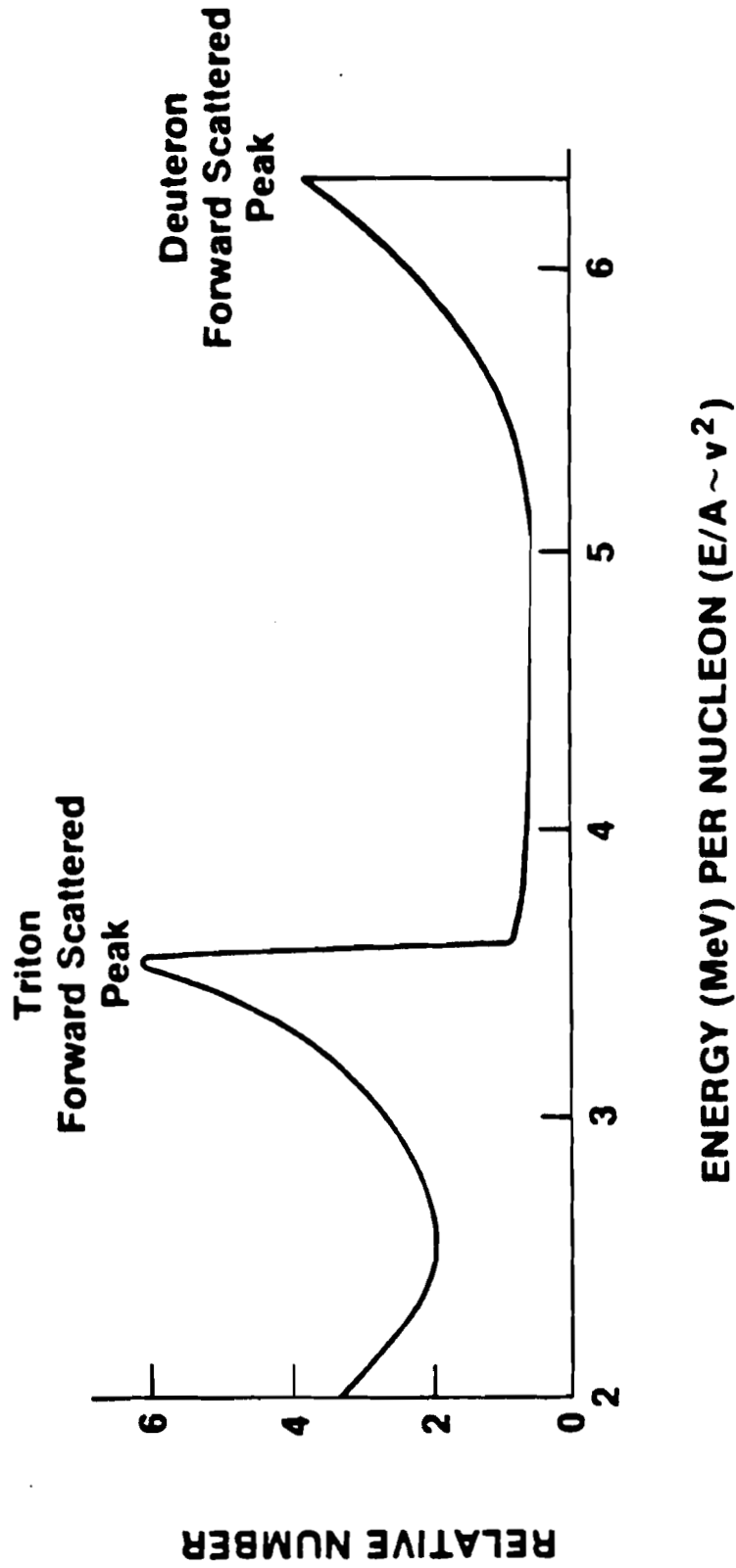
where  $\sigma_D$  and  $\sigma_T$  have been taken equal to .62 and .92 barns,<sup>2</sup> respectively.

Unlike the fusion reaction products, the knock-on particles have a wide range of possible energies. The knock-on spectrum is shown in Figure 1.2. The maximum knock-on energies occurring at 10.6 and 12.5 MeV represent the forward-scattered tritons and deuterons. Between these peaks is a region sparsely populated and with little structure. Measurements of the particle spectrum in this region shows a distribution consistent with the knock-on spectrum.

The knock-on particles can best be counted by using thin CR-39 solid state track detectors. These detectors have nearly 100% counting efficiencies over a wide velocity interval<sup>3</sup> and insensitive to x-rays and electron backgrounds if doses are less than 10 Mrad.<sup>4</sup>

Details explaining the process by which these detectors record charged particles are given in Appendix A. Basically, they operate as follows: As a charged particle enters the detector, its electric field alters the local chemical properties of the detector by breaking chemical bonds around its trajectory. Upon chemical etching, these alterations etch more quickly than the surrounding bulk material resulting in the formation of pit structures called "tracks." For a given charge  $Z$ , measurement of the track diameter determines the particle velocity or equivalently its energy-per-nucleon (i.e.,  $E/A$  where  $E$  is the particle energy divided by its nucleon number,  $A$ )<sup>5</sup>

Data reduction is currently complicated by the presence of a particle background and the inability of the detector to separate protons from knock-on particles over all velocities. If a stopping



E1663

Figure 1.2

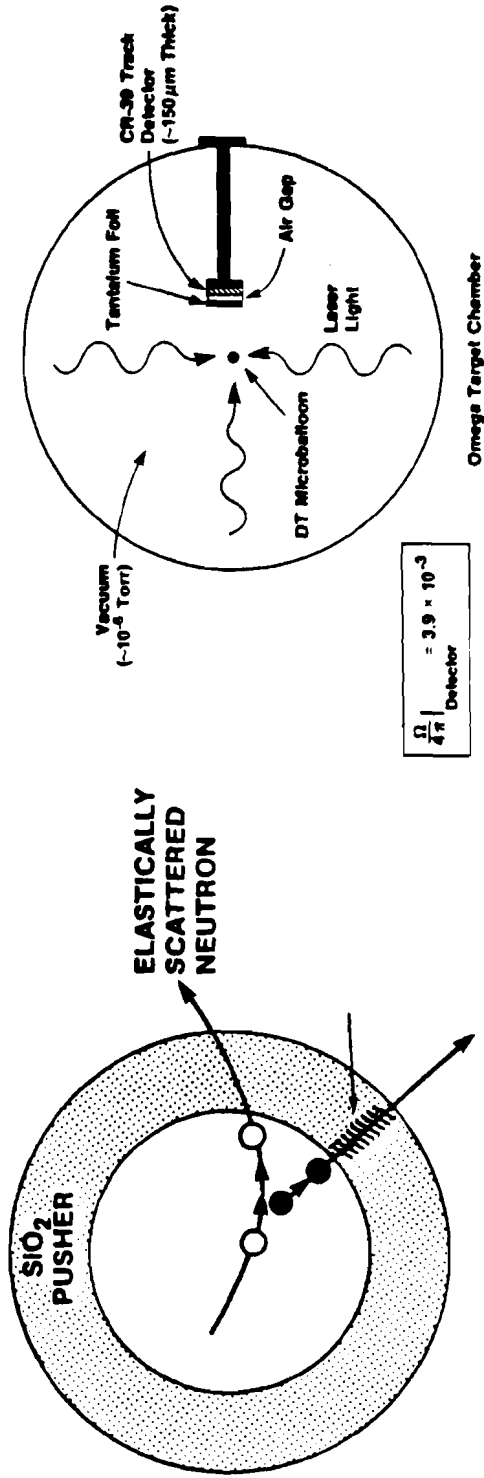
foil is not placed in front of the detector, the ion blowoff from the target will be many orders of magnitude larger than the knock-on signal thus being irretrievably lost in the myriad of overlapping background tracks. In the present experiments a 50  $\mu\text{m}$  tantalum stopping foil is placed in front of the detector, as shown in Figure 1.3. This was also greater than the 40  $\mu\text{m}$  of tantalum which is required to additionally stop the 3 MeV DD protons. An air gap shown in the figure is required to prevent degradation of the track detector sensitivity when placed in vacuum.

The tantalum foil does not stop energetic protons above 3 MeV or protons produced in the tantalum foil or track detector from producing tracks on the detectors. This background must be separated from the knock-on tracks by employing various track criteria. This background is most serious to deal with since knock-on tracks can have comparable track diameters with the background tracks. As track diameter gives information only of particle velocity, the particle range is additionally required to determine its nucleon number. Range information is deduced from "spatial coincident track pairs" where a track is produced on both the entrance and exit sides of the detector. The presence of such structures over a predetermined diameter interval can be used to separate protons which produce non-coincident tracks from knock-on particles which produce coincident tracks.

The finite interval of track diameters results in a limitation of the detectability over which the detector can discriminate against protons. Therefore, if  $\Gamma_d$  and  $\Gamma_t$  represent the fraction of knock-on



# KNOCK-ON DIAGNOSTIC



E1055

Figure 1.3

deuterons and tritons which fall into the discrimination range of the detector, then the number of spatial coincident tracks observed is given by

$$Q = (\sigma_d \Gamma_d n_d R + \sigma_t \Gamma_t n_t R) \frac{\Omega}{4\pi} Y_n \quad (I-5)$$

where  $\frac{\Omega}{4\pi}$  is the fractional solid angle subtended by the track detector.

Determination of  $\Gamma_d$  and  $\Gamma_t$  are the major theoretical uncertainties in the measurement. For target  $\rho R$  conditions less than 4 mg/cm<sup>2</sup> these parameters can be simply determined by knowing (1) the energy interval over which the detector can separate the proton background and (2) the differential cross section for each of the two knock-on processes.<sup>6</sup>

In future experiments when target  $\rho R$  conditions exceed 4 mg/cm<sup>2</sup> further uncertainties in  $\Gamma_d$  and  $\Gamma_t$  will exist. Here spectral distortion due to the slowing down of the knock-on particles through the target alters the shape of the spectrum and thus changes  $\Gamma$ . Two methods have been examined to correct for these distortions. One method relies on the measured energy loss of DD protons. Since these protons have velocities comparable to that of the forward-scattered tritons, they can be used to probe the localized distortion of the triton peak. This method breaks down above 10 mg/cm<sup>2</sup> where the protons are stopped inside the target. The second method requires the use of two detectors to view two adjacent energy intervals across the spectrum. The ratio of knock-ons from

each interval can be used to estimate the local distortion and thus correct  $\Gamma$  accordingly. This method can be used to about  $80 \text{ mg/cm}^2$  where, at this point, the knock-on particles are stopped inside the target. This knock-on method therefore cannot be utilized to break-even conditions, but for the near term laser fusion program it can be cheaply and easily implemented in diagnosing compression experiments.

Unlike many other indirect methods, the targets do not have to be specially prepared in order to use the technique. The only requirement is that a DT fuel mixture be present to produce the necessary 14 MeV neutrons. Deuterium-filled microballoons are not acceptable targets for this diagnostic since the DD neutrons are not energetic enough to produce the required knock-on energies to separate them from the DD protons.

### C. Alternative Methods In Measuring Fuel $\rho R$

Various methods have been proposed to measure fuel  $\rho R$ . These include (1) neutron activation of the tamper material by the DT neutrons,<sup>7</sup> (2) Stark broadening of seed material initially mixed in the fuel,<sup>8</sup> (3) DT-to-DD reaction ratio for deuterium-filled targets,<sup>9</sup> and (4) intensity measurements of the  $K\alpha$  x-ray radiation produced by the scattering of charged particle fusion products off high Z seed material in the fuel.<sup>10</sup> Each method has its distinct inherent difficulties, as will be discussed below.

## 1. Neutron Activation

Figure 1.4 shows the basis physics of this diagnostic. Here a 14 MeV neutron interacts with a  $^{28}\text{Si}$  nuclide producing a proton and excited  $^{28}\text{Al}^*$  nuclear state. This state decays first by  $\beta^-$  emission (whose endpoint energy is 2.86 MeV) to  $^{28}\text{Si}^*$  having a half-life of 2.24 minutes, which then  $\gamma$ -decays. To reduce background counts both  $\beta^-$  and  $\gamma$  rays are counted in coincidence. (The intermediate state has a half-life of only 0.5 ps.)

The number of activated nuclei  $N^*$  is given by

$$N^* = \sigma Y_n n_{\text{Si}} \Delta R \quad (\text{I-6})$$

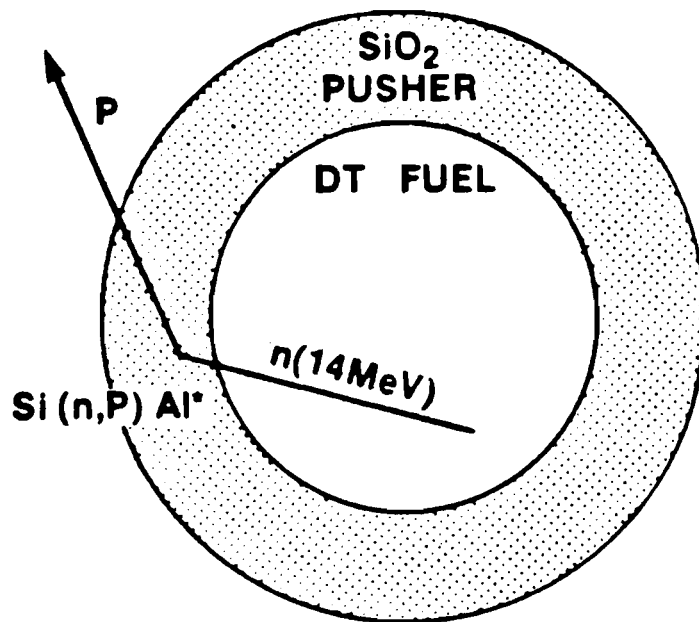
$$\text{where } n_{\text{Si}} = \rho \frac{A_n}{M} \quad (\text{I-7})$$

The parameter  $n_{\text{Si}}$ ,  $\Delta R$ ,  $A_n$ ,  $\rho$ , and  $M$  are the silicon number density, pusher-tamper thickness, Avogadro's number, glass density and the atomic mass, respectively. Therefore, the number of activated nuclei can be directly related to the tamper  $\rho R$  by

$$N^* = \frac{0.6 \sigma (\text{barns})}{A} Y_n (\rho \Delta R) \quad (\text{I-8})$$

The (n,P) cross section for  $^{28}\text{Si}$  is 0.25 barns. It is therefore less efficient per DT neutron than with the knock-on method

Neutron Activation



'RAD CHEM'

Figure 1.4

which uses the cross sections of 0.62 and 0.92 barns for the deuteron and triton, respectively.

It should be noted that  $N^*$  is not the detected count but rather the total number of activated nuclei. Typically, a five-minute sampling time is taken to obtain adequate counting statistics. This, in turn, increases the threshold value still further.

Another limitation of this technique is that it does not measure the fuel  $\rho R$  directly but must rely on numerical simulation to infer this from the tamper conditions. Only in extreme cases of spherical symmetry, uniform density in both the fuel and pusher-tamper, and thin shell can the initial parameters and measured compressed tamper  $\rho R$  give exact results for the compressed fuel  $\rho R$ ; namely,

$$(\rho R)_{f_c} = (\rho R)_{f_o} \frac{(\rho \Delta R)_p}{(\rho \Delta R)_p} \quad (I-9)$$

where  $(\rho R)_{f_o}$ ,  $(\rho R)_{f_c}$ ,  $(\rho \Delta R)_p$ , and  $(\rho \Delta R)_p$  are respectively the initial and compressed  $\rho R$  of the fuel and pusher-tamper. These assumptions are not met in laser fusion targets and therefore density modeling is necessary to extract fuel  $\rho R$  conditions.

## 2. Stark Broadening

The width of spectral lines under certain conditions give direct information of the local density where they are produced. This in turn can be used to estimate the fuel  $\rho R$ . Four basic

mechanisms can produce spectral broadening. These are listed below:

- (1) Natural
- (2) Doppler
- (3) Collisional (Stark)
- (4) Zeeman

The first broadening mechanism is inversely proportional to the lifetime of the state (result of Heisenberg uncertainty principle). No density information is obtained by this process. The second mechanism, Doppler broadening, increases the line-width due to the random thermal motion of the emitting atoms. Again no density information is obtained by this mechanism. However, for Stark broadening the local electric field of neighboring atoms can alter the states enough so that the energy levels are smeared. The degree of smearing (which is Lorentzian in shape) gives direct information of the local density. That last process of Zeeman splitting is relevant only when magnetic fields are present. This process has as yet not been identified from laser fusion targets.

Therefore, useful density information can be extracted from only Stark broadening. This has been done by placing Ne inside the target. However, the task of unfolding this broadening component from Doppler broadening is a non-trivial task. In addition, this method breaks down at fuel densities on the order of 1 to 2 mg/cm<sup>3</sup> where the spectral lines begin to overlap. The possibility of using argon in place of neon has been suggested, but higher temperatures are required.

Still another difficulty arising from this method is that the atoms may radiate at times significantly different from the time when the thermonuclear burn occurs. Thus measured fuel  $\rho R$  values may not characterize the fuel conditions during the time of neutron production.

### 3. Measurement of DT-to-DD Reaction Ratio

The ratio of DT neutrons to DD neutrons gives direct measurement of the fuel  $\rho R$  for tritium-free targets. In one of two possible DD reaction channels a 1 MeV triton is produced. As the triton travels through the fuel the probability of causing a DT reaction is proportional to the deuteron number density (and therefore the fuel density) and the distance traveled through the fuel. There, however, exist three limitations of this method. These are:

- (1) the analysis can only be used for tritium-free targets,
- (2) the detection efficiency is limited by the neutron detection efficiency and
- (3) large uncertainties in the ratio result for fuel  $\rho R$  conditions greater than  $10^{-2} \text{g/cm}^2$  when ion fuel temperatures are less than 5 KeV.

Direct detection of the DD protons and the DT alpha particles result in high detection efficiency. Unfortunately, for target  $\rho R$  conditions greater than  $10^{-3} \text{g/cm}^2$  the alpha particles are stopped within the target and above  $10^{-2} \text{g/cm}^2$  the DD protons are also stopped



in the target. Therefore, the detection of neutron reaction products will be necessary for target conditions in excess of  $.001 \text{ g/cm}^2$ .

Limitation (3) is the result of the fact that the beam average reaction rate  $\langle \sigma v \rangle_b$  is a very sensitive function of ion temperature below 5 KeV, as shown in Figure 1.5 (taken from reference 9).

The fuel  $\rho R$  can be measured in a very similar manner by the ratio of DD neutrons to  $D^3H_e$  protons from deuterated targets. The chief limitation here is that the  $D^3H_e$  has a much smaller beam reaction rate compared to the DT beam reaction rate.

#### 4. Intensity Measurement of $K\alpha$ X-Ray Lines

Fusion products, in particular DT alpha particles and DD protons, can be used to produce K-shell x-rays from seeded materials initially mixed in the fuel. The number of such x-rays is proportional to the fuel  $\rho R$ . Figure 1.6 shows that the cross section falls rapidly with increasing Z of the seed material. However, low Z seed material cannot be arbitrarily used because of the presence of a large x-ray background resulting primarily from bremsstrahlung from the target shell. Typical data of the x-ray background from the Zeta Laser System show that a reasonable seed material should have a  $K\alpha$  energy of greater than 8 KeV. This requires a Z of 30 or higher. Such high Z materials can have detrimental effects on the target performance. If the concentration is too high, excessive radiation cooling of the fuel can degrade the thermonuclear performance and overestimate realistic target compressions for strictly DT-filled targets. The opposite extreme of low seed concentration may result in insufficient

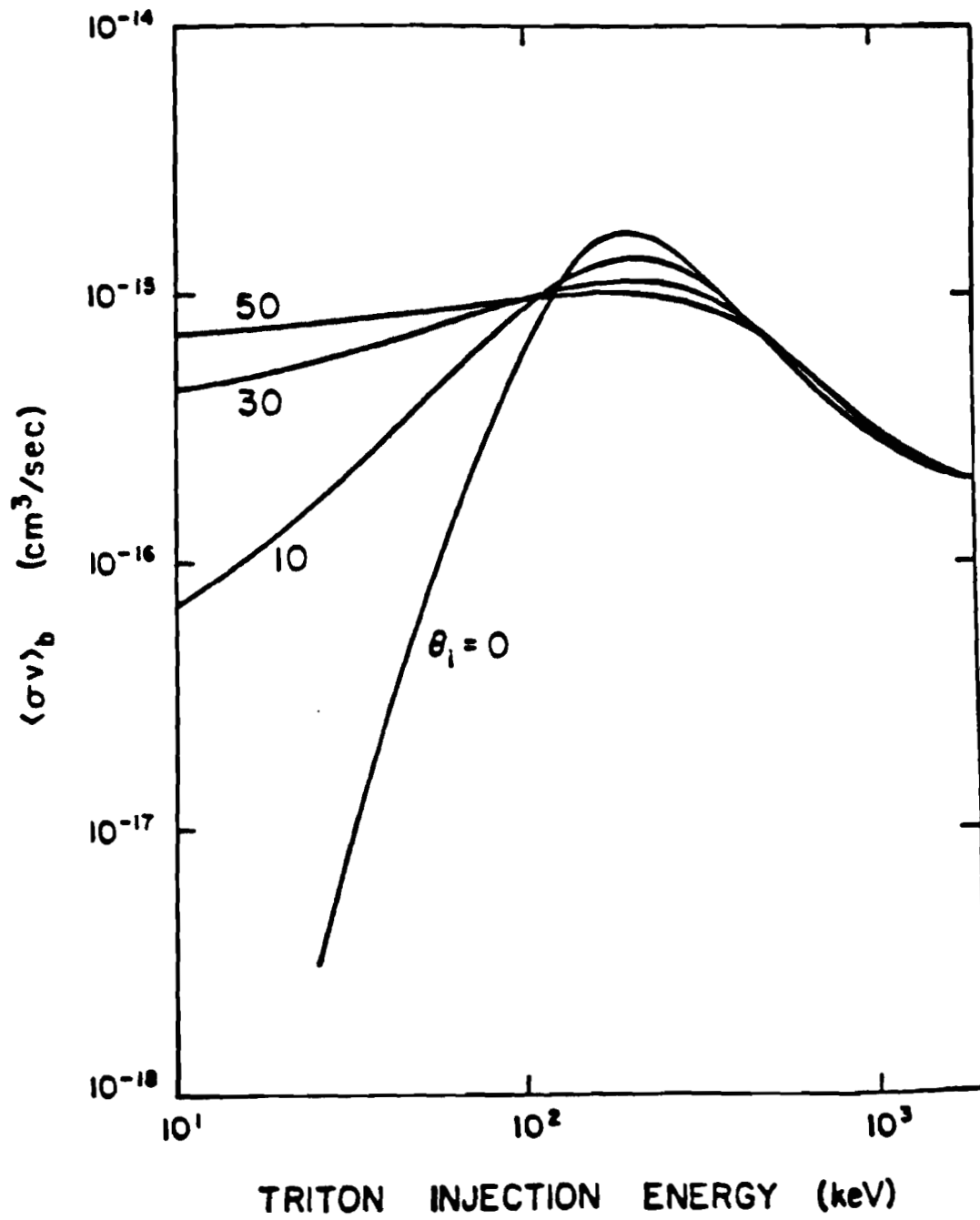


Figure 1.5

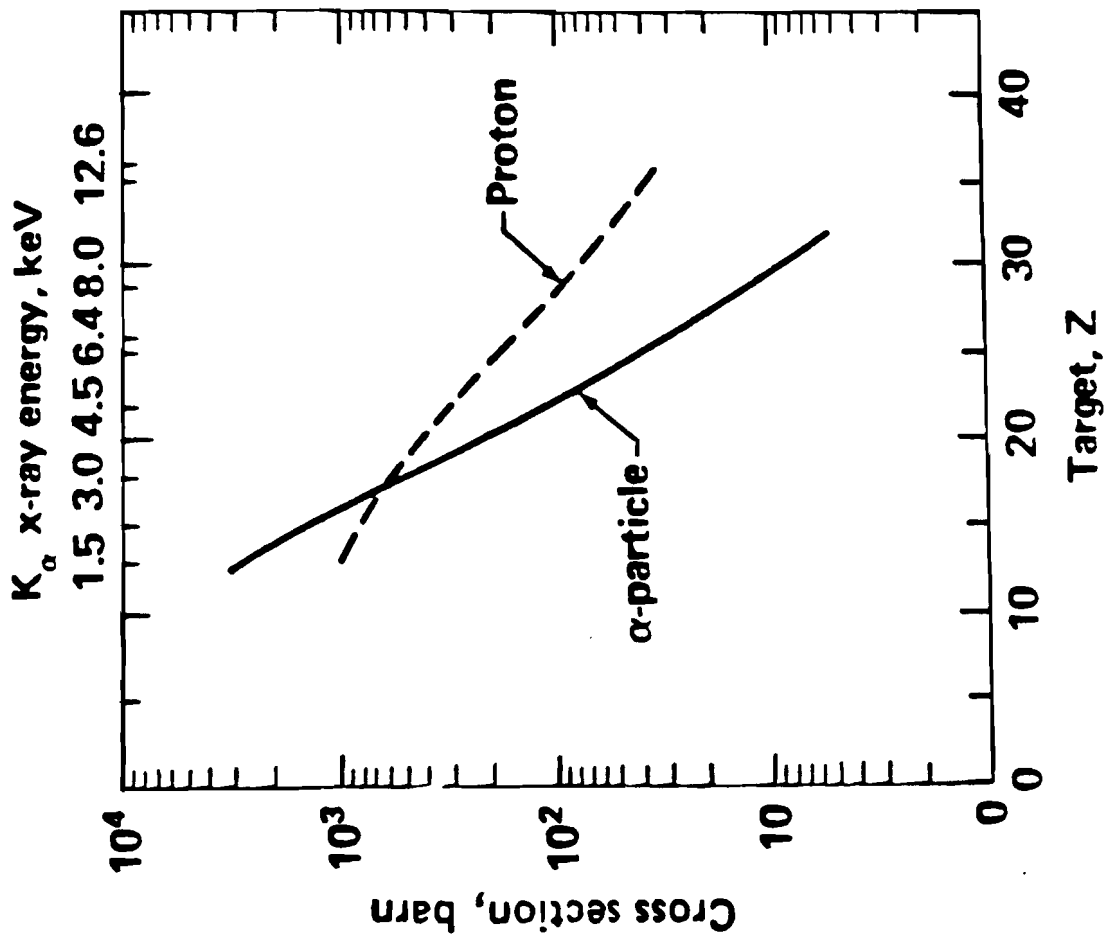


Figure 1.6

$K\alpha$  intensity to be easily separated from the x-ray background. In either case, specially prepared targets will be required to diagnose the fuel  $\rho R$  conditions.

A second method which uses  $K\alpha$  emission to measure compression is by measuring the dimension of the emission region using an x-ray pinhole camera. It is easily shown assuming uniform density and conservation of mass that

$$(\rho R)_f = (\rho R)_o \left(\frac{R_o}{R_f}\right)^2 \quad (I-10)$$

where  $(\rho R)_f$ ,  $(\rho R)_o$  and  $\left(\frac{R_o}{R_f}\right)$  are the final and initial fuel  $\rho R$  and the initial-to-final fuel radii, respectively. Notice that measurement uncertainty in  $R_c$  will result in a two times larger uncertainty in the fuel  $\rho R$  estimate. For example, if the compressed fuel has a dimension of 20  $\mu\text{m}$  and the spatial resolution is 5  $\mu\text{m}$ , the fuel  $\rho R$  uncertainty is  $\pm 50\%$ .

This procedure suffers from the same limitation as mentioned above when the  $K\alpha$  intensity lines are measured.

#### D. Conclusions

Because the methods described above have a number of inherent difficulties, such as tamper density modeling, utilization of specially prepared targets, and high threshold and resolution limitations, the knock-on diagnostic has been developed at the University of Rochester's Laboratory for Laser Energetics. This diagnostic has

the lowest detection threshold compared with all other alternative methods and does not rely on modeling of tamper conditions. In addition, standard DT-filled targets can be used with this method.

## II THE SIGNIFICANCE OF FUEL $\rho R$

### A. Chapter Overview

Estimates for establishing breakeven requirements, fractional DT burn, and self-heating of the fuel will be shown to be strongly dependent on the fuel  $\rho R$  conditions. Emphasis will be placed on the derivation of analytical models to clarify the relevant physical principles. These models have a number of simplifications which can only be treated properly with the use of complex numerical codes involving transport phenomena, ablation, hydrodynamic and nuclear burn. The goal of this chapter is to discuss the qualitative importance in which  $\rho R$  enters into these estimates and in doing so stimulates additional discussion by an increased number of researchers in this field.

The chapter will be divided into three sections. In section B, a model will be presented for the fuel conditions required to achieve breakeven conditions. Here it will be shown that the required fuel  $\rho R$  depends primarily on the fuel temperature and has a minimum at about 20 KeV. As will be discussed, this minimum is the result of two competing processes: the reaction rate and radiation loss due to Bremsstrahlung.

Section C will examine the dependence of fractional burn on  $\rho R$ . Included here is an estimate of the disassembly time of the target based on the time required for a rarefaction wave to travel from the target surface to its center. This estimate is then used to















































